

## Article

# The Development of WC-Based Composite Tools for Friction Stir Welding of High-Softening-Temperature Materials

Mohamed M. Z. Ahmed <sup>1,2,\*</sup> , Waheed S. Barakat <sup>3</sup>, Abdelkarim Y. A. Mohamed <sup>3</sup>, Naser A. Alsaleh <sup>4</sup> and Omayma A. Elkady <sup>5</sup>

- <sup>1</sup> Mechanical Engineering Department, College of Engineering at Al Kharj, Prince Sattam Bin Abdulaziz University, Al Kharj 16273, Saudi Arabia
- <sup>2</sup> Department of Metallurgical and Materials Engineering, Faculty of Petroleum and Mining Engineering, Suez University, Suez 43511, Egypt
- <sup>3</sup> Mechanical Department, Faculty of Technology and Education, Suez University, Suez 43511, Egypt; Wahed.saied@suezuni.edu.eg (W.S.B.); Abdelkarim.Mohamed@ind.suezuni.edu.eg (A.Y.A.M.)
- <sup>4</sup> Department of Mechanical Engineering, College of Engineering, Al Imam Mohammad Ibn Saud Islamic University, Riyadh 11432, Saudi Arabia; naalsaleh@imamu.edu.sa
- <sup>5</sup> Powder Metallurgy Division, Manufacturing Technology Department, Central Metallurgical R&D Institute (CMRDI), Cairo 11421, Egypt; o.alkady68@gmail.com
- \* Correspondence: moh.ahmed@psau.edu.sa; Tel.: +966-011-588-1200

**Abstract:** This work presents a detailed investigation for the effect of  $Y_2O_3$  and Ni additions on the densification behavior, microstructural evolution and mechanical properties of a WC-Co-TaC-NbC composite. With the aim of obtaining WC-based composites with improved fracture toughness, to be used in severe conditions of high-temperature deformation, different concentrations of  $Y_2O_3$  were incorporated with and without 5 wt% Ni addition. The consolidated composites were characterized using density measurement, XRD, SEM, hardness, fracture toughness, transverse rupture strength and compression testing. Fully dense composites were obtained through the applied consolidation regime of cold compaction and sintering at 1450 °C for 1.5 h under vacuum with a relative density up to 97%. The addition of 2.5 wt%  $Y_2O_3$  to the base WC composite increased the relative density and then slightly decreased with the increase of the  $Y_2O_3$  content. The addition of 5 wt% Ni to the base composites significantly increased the relative density to 97%. The XRD results indicated the existence of the  $Co_3W_3C$   $\eta$ -phase after sintering, and the intensity of its peaks was reduced with the addition of 5 wt% Ni. The microstructure of the consolidated composites consisted of three phases: WC,  $Co_3W_3C$  and  $Y_2O_3$ . The area fraction of the  $Y_2O_3$  phase increased as its weight fraction increased. In terms of the fracture toughness, the transverse-rupture strength (TRS) and the compressive strength were significantly improved by the addition of 5 wt% Ni with the 2.5 wt%  $Y_2O_3$ . Accordingly, this composition was used to manufacture the tools for the friction stir welding of the high-softening-temperature materials, which was successfully used for 25 plunges and about 500 cm of butt joints in nickel-based and carbon–steel alloys.

**Keywords:** WC-based composites; powder metallurgy; consolidation; microstructure; fracture toughness; friction stir welding



**Citation:** Ahmed, M.M.Z.; Barakat, W.S.; Y. A. Mohamed, A.; A. Alsaleh, N.; Elkady, O.A. The Development of WC-Based Composite Tools for Friction Stir Welding of High-Softening-Temperature Materials. *Metals* **2021**, *11*, 285. <https://doi.org/10.3390/met11020285>

Academic Editor: Hoon-Hwe Cho  
Received: 23 January 2021  
Accepted: 3 February 2021  
Published: 6 February 2021

**Publisher's Note:** MDPI stays neutral with regard to jurisdictional claims in published maps and institutional affiliations.



**Copyright:** © 2021 by the authors. Licensee MDPI, Basel, Switzerland. This article is an open access article distributed under the terms and conditions of the Creative Commons Attribution (CC BY) license (<https://creativecommons.org/licenses/by/4.0/>).

## 1. Introduction

Hard metals or cemented carbides are composite materials with one or more hard but relatively brittle carbide phases that are bonded together by a soft and ductile binder such as Co, Ni and Fe [1]. These composites are used in cutting tools, metal forming dies, mining tools and wear-resistant surfaces [2,3] due to their unique combination of mechanical, tribological and physical properties [4–6].

Tungsten carbide-cobalt (WC-Co) is one of the most important cemented carbides. It is mainly prepared by liquid-phase sintering, in which cobalt is the binder phase due to the

low interfacial energy between WC and Co, which leads to nearly perfect wetting and very good adhesion [5]. During sintering, liquid Co dissolves a certain amount of WC, and after saturation of liquid Co with WC during cooling, precipitation and growth of WC crystals take place, leading to the well-characterized microstructure of these composites [6].

Properties of WC-Co composites can be improved by reducing the WC grain size to sub-micrometer or nanometer scales [7]. In the last decade, many studies have focused on the high-performance hard materials, and considered WC-Co cemented carbides as ultrafine grained and nanocrystalline [8–12]. However, WC grain growth occurs during conventional pressureless sintering, especially in the case of liquid phase sintering [13]. Much effort has been made, and many ongoing studies are focused on developing full densification at a lower sintering temperature within a shorter thermal cycle, such as microwave sintering [8], hot pressing [9] or spark plasma sintering (SPS) [4]. The most successful method to control the WC grain growth is the addition of less than 1 wt% of inhibitors, such as TaC, ZrC, VC, Cr<sub>3</sub>C<sub>2</sub>, NbC, Y<sub>2</sub>O<sub>3</sub> or TiC, to WC-Co powder mixtures. This is useful for protection from any oxidation [7,14–16], inhibits heterogeneous grain growth and increases the hardness [16,17].

A combination of WC-Co with TiC, NbC or TaC can improve its high-temperature properties, such as oxidization resistance, hot hardness, strength, and high thermal and chemical stability [12,18]. Yu et al. [14] have demonstrated that the sintering of ultrafine WC-10%Co cemented carbide with 1% TaC or 1% NbC in vacuum furnace at 1400 °C for 1.5 h leads to maximum hardness and transverse-rupture strength. The sintering of ultrafine WC-10%Co composite with 1% NbC in a vacuum furnace at 1400 °C for 1h also improves the hardness and fracture toughness [15]. Other researchers found the maximum mechanical properties can be obtained by adding 1% NbC [19,20]. Also, dispersion of nano-grained second-phase particles within the matrix or along the grain boundaries of the micron and/or submicron-sized matrix material leads to a significant improvement of strength and fracture toughness by the order of two to four times, compared with the conventional composite materials [21].

Metallic binder (Co) is introduced to improve WC composite inter-particle bonding and toughness. However, metallic binders reduce the hardness and corrosion/oxidation resistance [22]. In addition, the transformation of Co to the hcp phase enhances grain growth. On the other hand, it is toxic and of high cost [23,24]. Therefore, efforts have been made to obtain harder materials with little amounts of Co and WC with no metallic binder. Another method of implementation is to use other metallic binders, such as Ni binder [17]. Ni addition can improve the WC-Co strength through solid solution strengthening [17].

Rare earth elements (REE) in conventional cemented carbides have shown beneficial effects on the TRS and toughness [25]. It has been reported that the addition of small amounts of REE element oxides to WC-Co enhances the wettability of Co and WC, refines the grains, controls the uneven grain growth and allows the formation of  $\eta$  phase in the cemented carbides [26]. Furthermore, the addition of 1.5 wt% REE oxides (Y<sub>2</sub>O<sub>3</sub>, La<sub>2</sub>O<sub>3</sub>–CeO<sub>2</sub>) to WC-10%Co cemented carbides produced a much finer grain size and better mechanical properties [16]. The addition of Y<sub>2</sub>O<sub>3</sub> and NbC to WC-Co alloys improves the hardness and fracture toughness of the ultrafine WC-Co alloys [7]. The addition of 5–20 wt% Y<sub>2</sub>O<sub>3</sub> to the cemented carbides increases the hardness and the fracture toughness of the 5 wt% Y<sub>2</sub>O<sub>3</sub>-WC/Co cemented carbide [27]. Recently, Qing et al. [28] investigated the effect of Y<sub>2</sub>O<sub>3</sub> on the microstructure and mechanical properties of tungsten carbide with 12 wt% cobalt prepared using a solid-liquid doping method and SPS. They reported that the existence of Y<sub>2</sub>O<sub>3</sub> hindered the growth of WC grains and the composite sample with 1.3 wt% Y<sub>2</sub>O<sub>3</sub> possessed maximum hardness and fracture toughness measured at 1446.9 HV and 11.9 MPa·m<sup>1/2</sup>. Yang et al. [29] prepared WC-8 Co composite powders doped with Y<sub>2</sub>O<sub>3</sub> by the wet chemical method and conducted the consolidation using by SPS at 1200 °C, 1250 °C and 1300 °C. They reported that the comprehensive performance of WC-8%Co cemented carbide doped with Y<sub>2</sub>O<sub>3</sub> was best at the sintering temperature of 1250 °C, with a hardness of 19.64 GPa and a fracture toughness of 11.97 MPa m<sup>1/2</sup>.

Li et al. [30] investigated the effect of mixing different amounts of  $\text{La}_2\text{O}_3$  with WC-10%Co and then conducted the consolidation using microwave sintering. They reported that the addition of an appropriate amount of  $\text{La}_2\text{O}_3$  can suppress WC grain growth and narrow the grain size distribution.

Based on the above literature, the addition of the REE oxides and the metallic elements are good candidates for WC-based composite improvement. Thus, the aim of this work is to study the effect of Ytria (0–10 wt%) and Ni (5 wt%) additions on the microstructure and mechanical properties of a WC-Co-NbC-TaC composite, and to examine the use of this composite material to manufacture friction stir welding tools for welding of high-softening-temperature materials.

## 2. Experimental Work

### 2.1. Materials

In this study, a powder of composition WC (93.35%), Co (6.5%) and TaC + NbC (0.5%) supplied by Guangzhou Hantangheng Trading Co., Ltd, China with a particle size ranging from 100 to 290  $\mu\text{m}$  was used as a base WC composite. Both  $\text{Y}_2\text{O}_3$  (Tung. Heavy Powder Inc., San Diego, CA, USA) and Ni powders with a 99.995% and 99.96% purity and a 2–3  $\mu\text{m}$  and 3–5  $\mu\text{m}$  particle size, respectively, were used as additive materials in the base WC composites. Figure 1 shows the SEM micrographs of the morphologies of the different starting materials. The main characteristics of the WC-Co-NbC-TaC,  $\text{Y}_2\text{O}_3$  and Ni powders are given in Table 1.

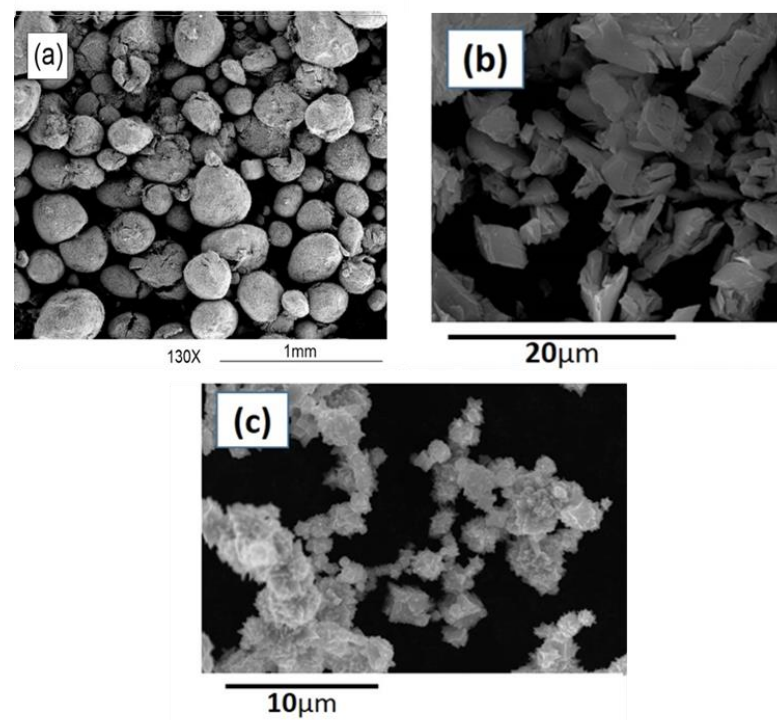


**Figure 1.** SEM micrographs for the morphology of the raw powders. (a) WC-Co-NbC-TaC, (b)  $\text{Y}_2\text{O}_3$  and (c) Ni.

**Table 1.** Properties of the WC-Co-NbC-TaC,  $\text{Y}_2\text{O}_3$  and Ni powders.

Powder	Purity %	Particle Size	Density $\text{g/cm}^3$
WC-Co-NbC-TaC	99.99	100–290 $\mu\text{m}$	15.223
$\text{Y}_2\text{O}_3$	99.995	2–3 $\mu\text{m}$	5.01
Ni	99.96	3–5 $\mu\text{m}$	8.9

## 2.2. Powder Compaction and Sintering

The raw base material composite (WC-Co-NbC-TaC) and that with the 5 wt% Ni addition were used as starting materials in this work. Different weight percentages of 0, 2.5, 5, 7.5 and 10 wt%  $Y_2O_3$  were added to both starting WC base composites. Table 2 gives the nominal chemical composition of the different composite batches investigated in this study. The required weight of powder for each batch was weighted and mixed in a SPEX ball mill with a 5:1 ball-to-powder ratio for 2 h. The milling process was carried out at room temperature and a rotation rate of 1080 rpm. The mixtures were mixed with 1.5 wt% paraffin wax as a lubricant to reduce friction during compaction. Liquid ethanol ( $C_2H_5OH$ ) was used as a process-controlling agent, and then the mixtures were dried at 80 °C for 30 min in the dry furnace. The mixed powders were then cold compacted using a Zwick/Roell 16-ton-capacity cylinder. The pressing assembly is schematically illustrated in Figure 2a. Two types of compact cross sections were produced: a square of 8 mm sides with a 15 mm height, and a rectangular 30 mm  $\times$  7.5 mm cross section. For that purpose, two dies were designed and manufactured from K110 tool steel. Figure 2b shows the rectangular cross section die component with 3-D models of the die and lower punch, and 2D drawings with dimensions. In order to minimize the pressing cracks and ease of sample ejection from the dies, a  $\sim 1^\circ$  taper was machined onto both die openings. The dies were also designed as two-piece parts, to allow easy removal for re-machining or replacement. The samples were compacted at 400 MPa to produce compacts for the post-processing and characterization. The compacted samples were sintered at 1450 °C for 1.5 h in a vacuum furnace according to the heat-treatment cycle illustrated in Figure 3.

**Table 2.** The nominal compositions and the mixture-rule-calculated theoretical density of the different batch samples (wt%) produced in this work.

Batch No.	$Y_2O_3$	Ni	(WC/Co/NbC/TaC)	Theoretical Density, gm/cm <sup>3</sup>
1	0.0	-	100	15.223
2	2.5	-	97.5	14.96768
3	5.0	-	95	14.71235
4	7.5	-	92.5	14.45703
5	10	-	90	14.2017
6	0.0	5	95	14.90685
7	2.5	5	92.5	14.65153
8	5.0	5	90	14.3962
9	7.5	5	87.5	14.14088
10	10	5	85	13.88555

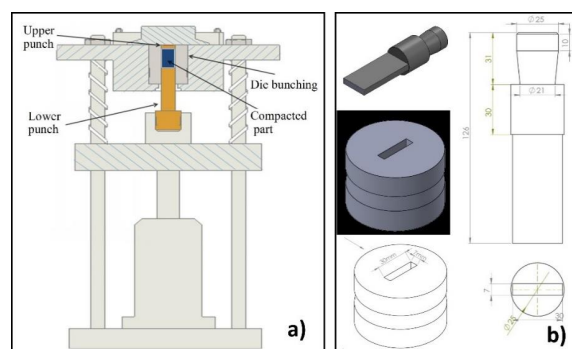


**Figure 2.** (a) Schematic drawing of the cold-compaction assembly. (b) 3D and 2D drawings of the rectangular die. All dimensions in (b) are in mm.

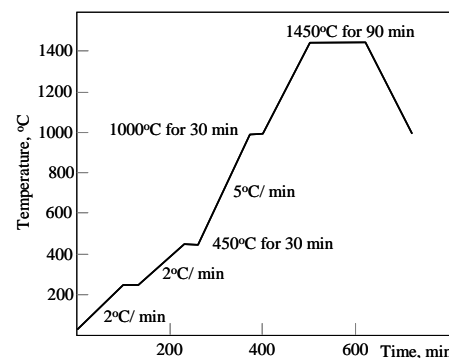


**Figure 3.** Heat-treatment thermal cycle applied in the compacted cemented carbide sintering process.

### 2.3. Characterization of the Consolidated Composites

Densification is one of the important parameters for the consolidated powder that determines the properties of the produced bulk materials. Densification is determined through the bulk density and the apparent porosity using the Archimedes method, taking distilled water as floating media according to the ASTM D1217 standard.

The consolidated samples were prepared through the standard metallographic procedures, first grinding with SiC grit papers of different grades up to 3000, and then mechanically polishing using 6  $\mu\text{m}$  and 3  $\mu\text{m}$  diamond paste. The microstructure of the different samples was investigated using a field emission gun scanning electron microscope (FEG-SEM, FEI company, Hillsboro, OR, USA) equipped with an EDS system (EDAX, AMETEK, Utah, Draper, South Pearl, CO, USA). X-ray diffraction (XRD) was used to identify the different phases that formed upon the consolidation process. We used an automated Siemens Model D-5000 diffractometer (Malvern Panalytical, Westborough, MA, USA) with Cu K-alpha radiation operated at 40 kV and 30 mA in the  $2\theta$  range of 20–100° at the step of 0.05°. The obtained XRD charts from the consolidated samples were compared with that of the mixed powder before consolidation.

Hardness measurements, fracture toughness, TRS and compressive-strength evaluations were used as the bases for assessing the mechanical properties of the composites. Vickers hardness operated at a load of 30 kg was used for the hardness test measurement. The fracture toughness was evaluated from the measurement of the total crack lengths produced at the opposite corners of a Vickers indent and the hardness of the samples based on the procedures given elsewhere [27,31]. The fracture toughness “ $K_{IC}$ ” was carried out on a polished surface of the hardness tester samples [32] under a load of 30 kg for a duration of 15 s. Calculation of the fracture toughness was carried out on the basis of the nature of the observed cracks, in which the crack length was measured using optical microscopy. There are two types of cracks, the palmqvist crack and the halfpenny crack. In the case of palmqvist cracks, the crack length was calculated based on the palmqvist shaped-crack model using the following Equations (1) and (2):

$$K_{IC} = 0.0515 P/c^{3/2} \quad (1)$$

However, in the case of halfpenny cracks, the crack length was calculated based on the halfpenny shaped-crack model using the following equation:

$$K_{IC} = 0.0726 P/c^{3/2} \quad (2)$$

where  $P$  is the indentation load (N), and  $c$  is the crack length measured from the middle of the Vickers indentation (m).

The TRS was determined according to the ISO 3327-1975 standard by using a specially designed three-point bending setup, which ensured accurate alignment and centering of the samples. The sample dimensions were 20 mm  $\times$  6.5 mm  $\times$  6.5 mm. Figure 4a shows the

bending setup during loading with an enlarged image. The samples were loaded to failure in an Instron testing machine. TRS is expressed in  $\text{N mm}^{-2}$  and is given in Equation (3):

$$\text{TRS} = \frac{3FL}{2Wh^2} \quad (3)$$

where  $F$  is the applied force to fracture,  $L$  is the distance between the two parallel supports,  $W$  is the width and  $h$  is the height of test specimen.



**Figure 4.** (a) The three-point bending setup, with an enlarged image of the measurement of the Transverse rupture strength (TRS) of the cemented carbide materials. (b) The compression-test system.

The compression strength of the consolidated samples was measured using an Instron universal testing machine with a 300 kN capacity. The cross-section area of the specimen was  $63.75 \text{ mm}^2$ , and the applied cross-head speed of the universal test machine was  $0.05 \text{ mm/s}$ . The test was conducted at room temperature. Figure 4b shows an image of the compression-testing setup.

### 3. Results and Discussion

#### 3.1. Densification

The bulk density of the consolidated samples was measured using the Archimedes method and divided by their corresponding theoretical density that was calculated according to the rule of mixture. Figure 5 shows the relative density of the WC-Co-TaC-NbC composite and WC-Co-TaC-NbC-5 wt% Ni with different weight percentages of  $\text{Y}_2\text{O}_3$ . Generally, it can be noted that the relative density exceeded 90%, and reached up to 97% for some samples, which indicated the effectiveness of the consolidation cycle in terms of cold compaction followed by sintering under vacuum at  $1450 \text{ }^\circ\text{C}$  for 1.5 h. It can be noted that the densification was improved through the addition of 5 wt% Ni. This can be attributed to the small particle size of the Ni particles, which can enhance the densification behavior during the cold-compaction stage through the filling of the small pores between the WC base composites that have a large starting particle size ( $100\text{--}250 \text{ }\mu\text{m}$ ). The Ni was also ductile phase, which improved the cold-compaction densifications. In addition, Ni has a low melting point, and can melt during the sintering process and enhance the liquid phase sintering process. As a result, the samples with 5 wt% Ni had a high density value relative to those free of Ni.

The addition of the  $\text{Y}_2\text{O}_3$  to both composites in different percentages clearly affected the densification behavior. The densification improved at the added value of 2.5 wt% and then slightly decreased. This can be attributed to the fine particle size ( $2\text{--}3 \text{ }\mu\text{m}$ ) of  $\text{Y}_2\text{O}_3$  used relative to the matrix starting particle size ( $100\text{--}250 \text{ }\mu\text{m}$ ). This small particle size can fill the small pores between the large WC particles during the compaction process. The slight decrease in the relative density by increasing the  $\text{Y}_2\text{O}_3$  higher than 5 wt% can be understood in terms of the  $\text{Y}_2\text{O}_3$  having a higher strength and a very high melting point, and which requires either a higher cold-compaction pressure and/or a high sintering

temperature to achieve the same relative density at the different wt%  $Y_2O_3$ . In addition, the lower density of both Ni ( $8.9 \text{ g/cm}^3$ ) and  $Y_2O_3$  ( $5.0 \text{ g/cm}^3$ ) compared to that of the WC composite ( $15.39 \text{ g/cm}^3$ ) caused a decrease in the overall density of the prepared samples. Alkady [27] reported the same behavior of a decrease in the relative density by increasing the nano-yttria additions more than 5 wt% in the WC-Co composites sintered at the same temperature and for a longer sintering time. Furthermore, the phases that formed during the sintering process might affect the bulk density of the produced composites in terms of their density relative to that of their constituents.

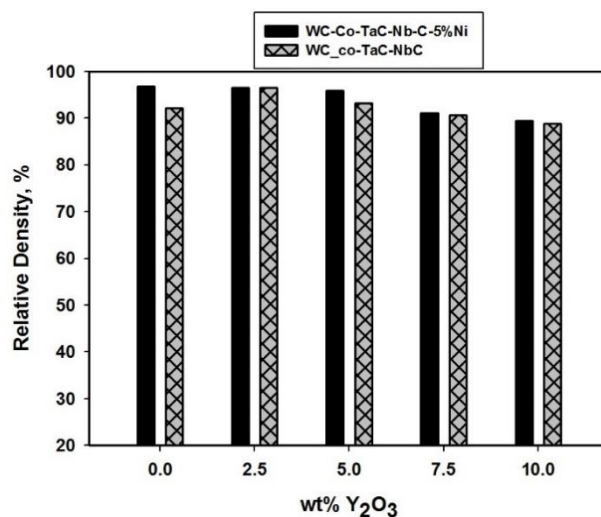


**Figure 5.** Relative density of the consolidated WC-Co-TaC-NbC and WC-Co-TaC-NbC-Ni-5 wt%) composites with  $Y_2O_3$  additions, from 0 wt% to 10 wt%.

### 3.2. XRD Analysis

The XRD patterns of the as-received WC-Co-NbC-TaC powder (WC\_AR) and ball milled powder (WC\_AM) sintered composites after addition of the different wt% of  $Y_2O_3$  are illustrated in Figure 6a, and the sintered composites after addition of 5 wt% Ni and different wt% of  $Y_2O_3$  are illustrated in Figure 6b. The red rectangles indicated on the charts are illustrated as enlarged areas to the right of the figures.

The starting WC-Co-NbC-TaC material (Figure 6a,b; WC\_AR) consisted of coarse polycrystalline grains, indicated by the sharp Bragg diffraction peaks. The effect of ball milling for 2 h (Figure 6a,b, WC\_AM) can be observed in the broadening of the WC peaks. This can be attributed to the grain refining and straining introduced by the high energy ball milling into the starting WC particles [33,34]. The XRD patterns after consolidation (Figure 6a, 0%  $Y_2O_3$ ) indicated the presence of a new phase peaks, which correspond to the  $\eta\text{-Co}_3\text{W}_3\text{C}$  phase. The  $\eta\text{-Co}_3\text{W}_3\text{C}$  phase is formed by diffusion during the sintering process at the expense of WC phase. It is formed at certain concentrations of WC and Co (about 6.5 wt%), starting from 750 °C up to 1400 °C, according to the WC-Co phase diagram [35]. The addition of the  $Y_2O_3$  enhanced the formation of the  $\eta\text{-Co}_3\text{W}_3\text{C}$  phase, as can be observed from the pronounced peaks in the XRD chart of the sample containing 2.5% (Figure 6a, 2.5%  $Y_2O_3$ ). The existence of the  $Y_2O_3$  peaks can only be observed at the highest wt% of the  $Y_2O_3$  content (Figure 6a, 10%  $Y_2O_3$ ). In terms of the effect of increasing the  $Y_2O_3$  content on the intensity of the WC matrix phase peaks, it can be observed that the intensity decreased systematically by increasing the  $Y_2O_3$  content, with the lowest peak intensities for the 10 wt%  $Y_2O_3$ . This could be attributed the reduction in the concentration of the WC in the matrix by the addition of  $Y_2O_3$  particles, as well as the formation of the  $\eta\text{-Co}_3\text{W}_3\text{C}$  phase.

The addition of 5 wt% Ni to the base composites (Figure 6b, 0%  $Y_2O_3$ ) resulted in a reduced peak intensity of the WC matrix phase and a significantly stronger peak intensity of the  $\eta\text{-Co}_3\text{W}_3\text{C}$  phase that was almost comparable to the WC peaks. In terms of the

sample with 2.5%  $Y_2O_3$  (Figure 6b), it can be noted that the addition of 5 wt% Ni affected the intensity of the  $\eta$ - $Co_3W_3C$  phase peaks, as their intensity was reduced significantly relative to that without the Ni addition (Figure 6a, 0%  $Y_2O_3$ ). This can be attributed to the effect of Ni in the liquid phase sintering, as the Ni melts and spreads around the WC phase matrix composite. The increase in the  $Y_2O_3$  content again resulted in the reduction of the WC phase peak intensity relative to the sample containing 2.5%  $Y_2O_3$ .

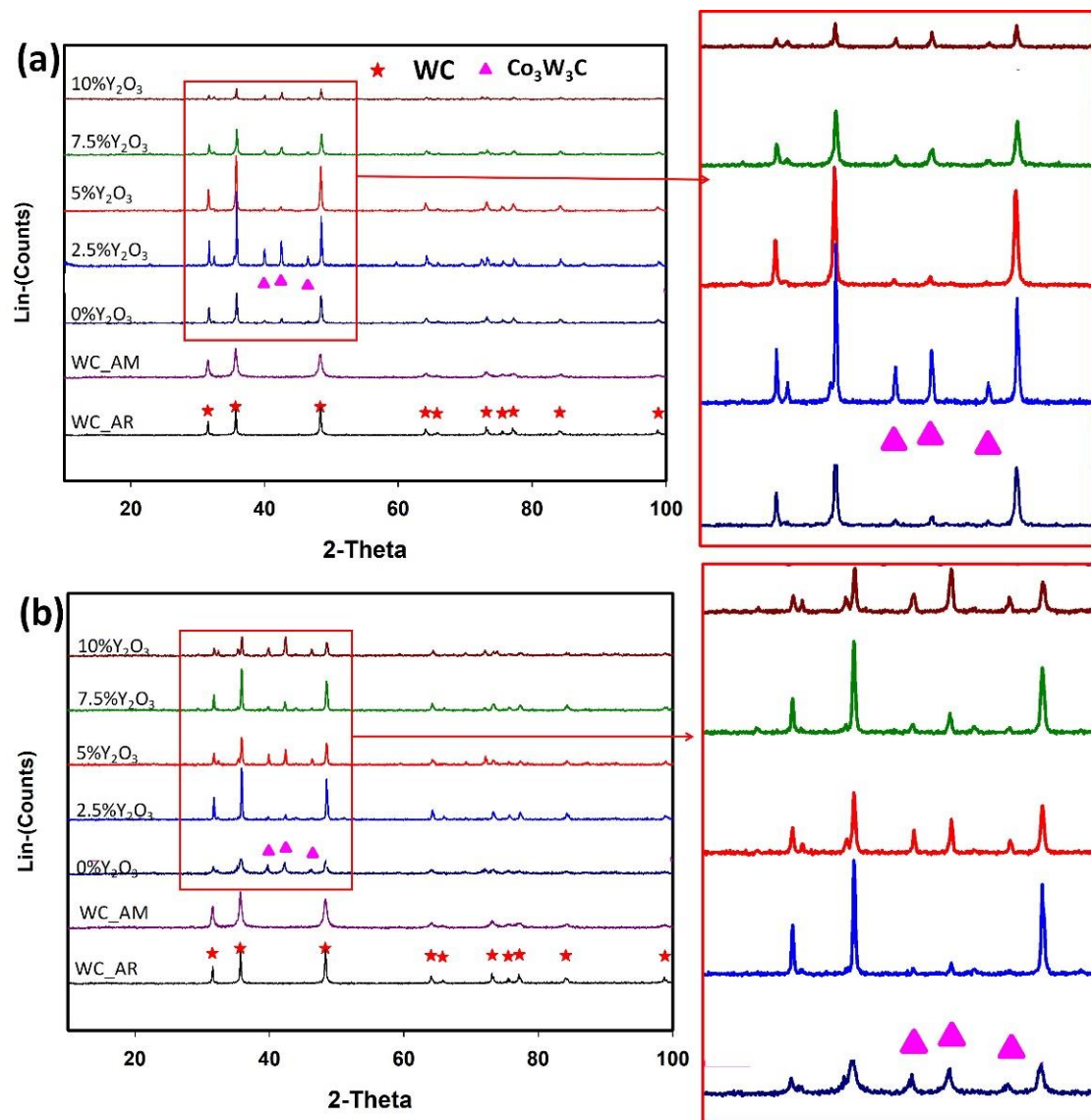
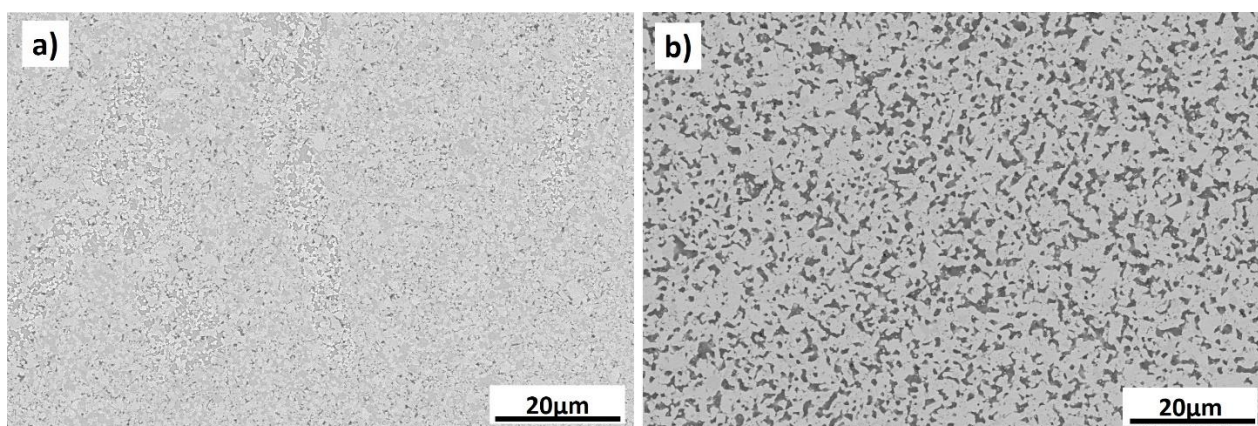


**Figure 6.** XRD patterns of the as-received (AR), as-milled (AM) powder after sintering of different composites. (a) WC-Co-TaC-NbC with different additions of  $Y_2O_3$ . (b) WC-Co-TaC-NbC with an addition of 5 wt% Ni and different additions of  $Y_2O_3$ . Enlarged areas for the indicated rectangles in each chart are illustrated to the right.

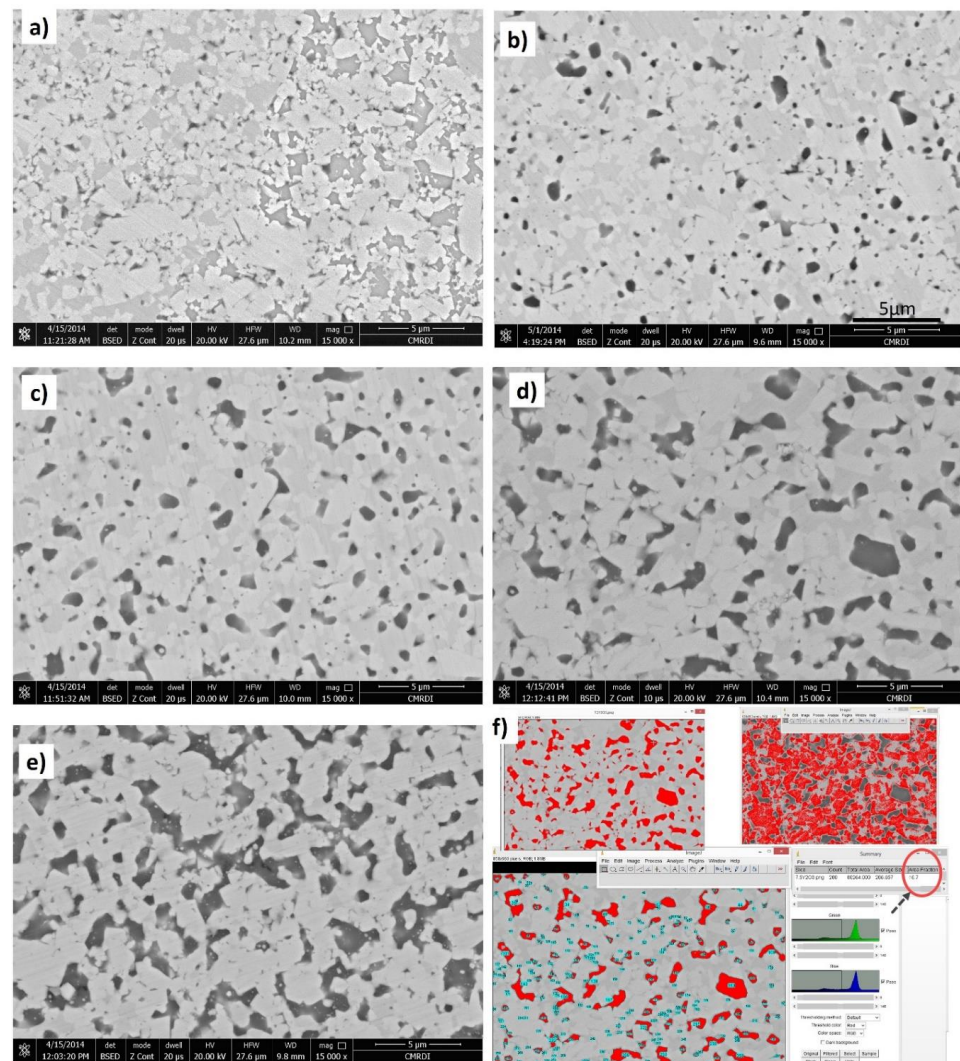
### 3.3. Microstructure of the Consolidated Composites

The microstructure of the consolidated composites was investigated using FEG-SEM, and Figure 7 shows an overview of the microstructure of the WC-Co-TaC-NbC consolidated base composites and with the 10 wt%  $Y_2O_3$  addition. This overview of the microstructure clearly indicates the effectiveness of the consolidation scheme applied in obtaining macrovoid-free samples. High magnification SEM micrographs of the consolidated composites with different wt%  $Y_2O_3$  added are illustrated in Figure 8. The microstructure the  $Y_2O_3$  free sample (Figure 8a) consisted mainly of two phases, a white

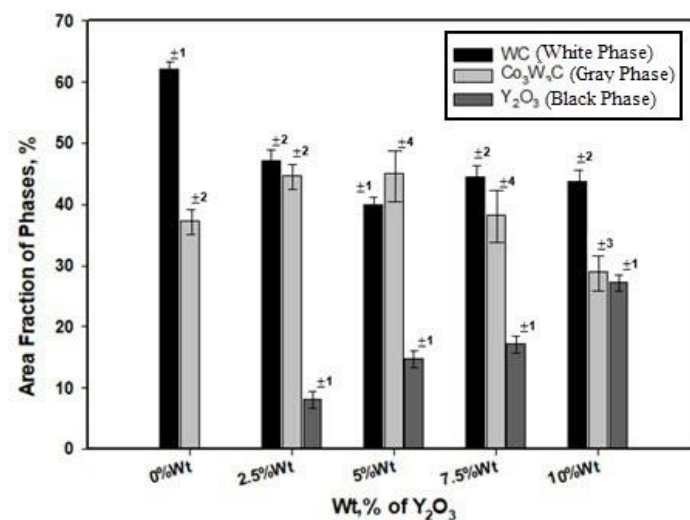
phase that belonged to the WC, and a gray phase that was found to be the  $\eta$  ( $\text{Co}_3\text{W}_3\text{C}$ ) phase formed between WC and Co during the sintering process, as indicated by the XRD results. The addition of the  $\text{Y}_2\text{O}_3$  particles to the base composite resulted in the appearance of a third phase that we named the black phase ( $\text{Y}_2\text{O}_3$  phase), as can be observed in the microstructure of the samples with different wt%  $\text{Y}_2\text{O}_3$  content: 2.5 wt% (Figure 8b), 5 wt% (Figure 8c), 7.5 wt% (Figure 8d) and 10 wt% (Figure 8e). It can be observed that the area fraction of this black phase increases with the increase of the  $\text{Y}_2\text{O}_3$  content. Figure 8f shows an example of the image processing carried out to calculate the area fraction of the three phases. The area fraction of the three existing phases calculated using image-processing software for the SEM micrographs is shown in Figure 8, and the results are presented as bar chart in Figure 9. The increase of the black ( $\text{Y}_2\text{O}_3$ ) phase was consistent with the  $\text{Y}_2\text{O}_3$  wt% increase. This increase was also at the expense of the other two phases,  $\text{Co}_3\text{W}_3\text{C}$  (gray) and WC (white). It should be mentioned that the density of the  $\text{Y}_2\text{O}_3$  was very low ( $\sim 5 \text{ gm/cm}^3$ ) relative to that of the WC-based composite ( $\sim 15 \text{ gm/cm}^3$ ). Thus the obtained area fractions from 8%, 14.8%, 16.7%, and 27% at 2.5 wt%, 5 wt%, 7.5 wt% and 10 wt%  $\text{Y}_2\text{O}_3$ , respectively, were consistent with this density difference between the WC-based composites and  $\text{Y}_2\text{O}_3$ . The process of consolidation that resulted in the current microstructural features can be explained as the following. The ball-milling process resulted in a homogenous distribution of the  $\text{Y}_2\text{O}_3$  particles in the WC matrix and in the refining of WC particles, and introduced a high amount of strain. The cold-compaction process preserved the homogenous distribution and the obtained characteristics of the powder. The green compacted samples consisted of a porous body with a relative density ranging from 55 to 60%, in which the particles of the WC-Co-TaC-NbC were in close contact with each other and surrounded by the  $\text{Y}_2\text{O}_3$  particles. During the sintering process, the  $\text{Co}_3\text{W}_3\text{C}$  was formed by diffusion at a high temperature that completes the consolidation process. During the sintering, the pores are closed, the WC particles change their shape and the binder phase spreads throughout the structure [27,36,37]. The final sintered structure was dense, consisting of faceted WC and  $\text{Co}_3\text{W}_3\text{C}$  grains with area fractions varied based on the  $\text{Y}_2\text{O}_3$  wt% addition (Figure 9).



**Figure 7.** SEM micrographs of the consolidated WC-Co-TaC-NbC. (a) 0 wt%  $\text{Y}_2\text{O}_3$ , (b) 10 wt%  $\text{Y}_2\text{O}_3$ .

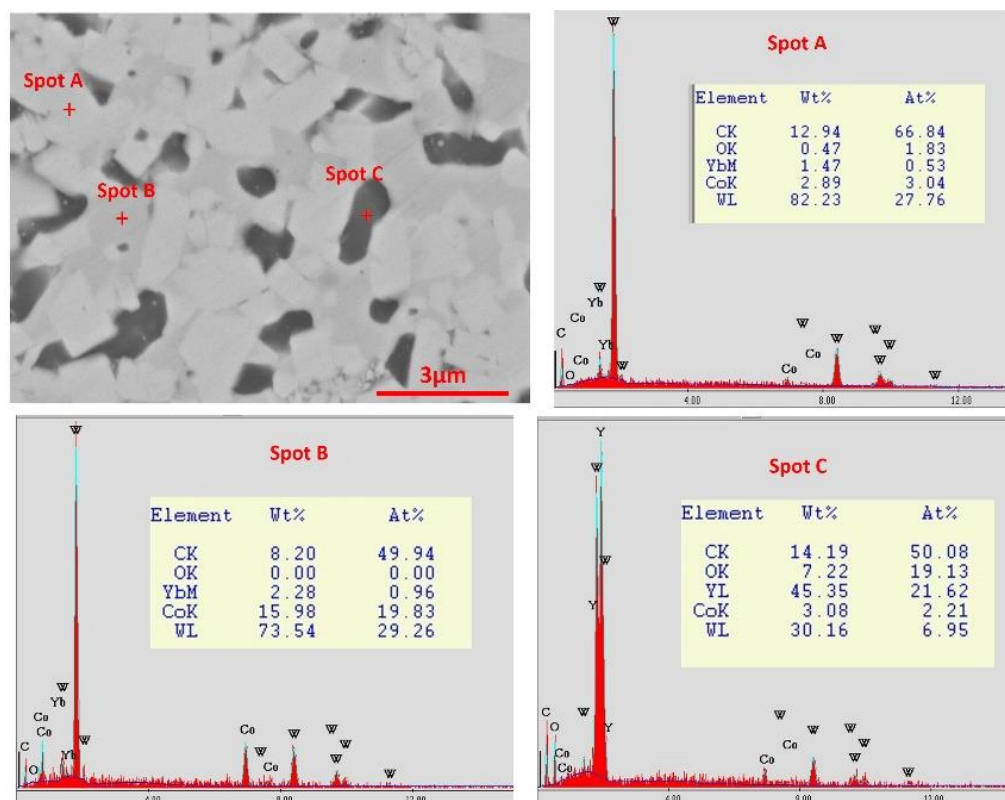


**Figure 8.** SEM micrographs of the consolidated WC-Co-TaC-NbC with different Y<sub>2</sub>O<sub>3</sub> content. (a) 0 wt% Y<sub>2</sub>O<sub>3</sub>, (b) 2.5 wt% Y<sub>2</sub>O<sub>3</sub>, (c) 5 wt% Y<sub>2</sub>O<sub>3</sub>, (d) 7.5 wt% Y<sub>2</sub>O<sub>3</sub>, (e) 10 wt% Y<sub>2</sub>O<sub>3</sub>, and (f) image processing of the SEM micrograph in (d) for area fraction calculation.



**Figure 9.** Bar chart of the area fraction of the three phases: WC (white phase), Co<sub>3</sub>W<sub>3</sub>C (gray phase), and Y<sub>2</sub>O<sub>3</sub> (black phase), calculated using image analysis of the SEM micrographs shown in Figure 8.

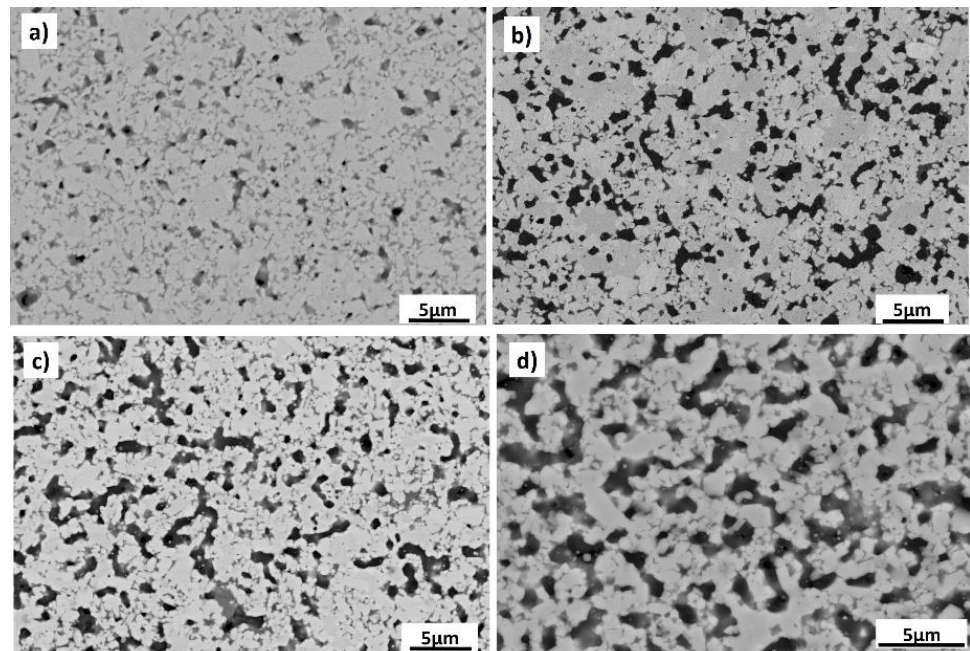
The EDS analysis of the different phases observed in the microstructure of the consolidated WC-based composites is given in Figure 10. The white phase (Spot A) consisted mainly of W, C with small amount of Co, and yttrium. The gray phase (Spot B),  $\eta$  ( $\text{Co}_3\text{W}_3\text{C}$ ), consisted of W, C and a high concentration of Co, which implies that this phase was formed upon the sintering process, as confirmed by the XRD results. The black phase (yttrium-containing) consisted of 45 wt% yttrium, 30 wt% W, 19 wt% O, 14 wt% C and a small amount of Co. These dark particles were mainly yttrium oxide ( $\text{Y}_2\text{O}_3$ ) added before the ball-milling, especially since the oxygen content was high and the W and C traces came from the WC particles behind the  $\text{Y}_2\text{O}_3$  particles.



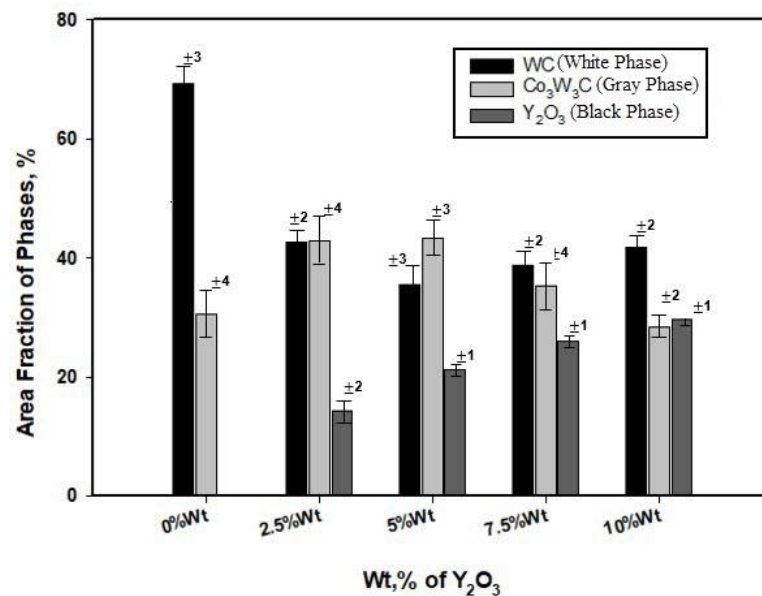
**Figure 10.** EDS analysis of the three phases observed in the consolidated WC-Co-TaC-NbC with 7.5 wt%  $\text{Y}_2\text{O}_3$ . Spot A = white (WC) phase; Spot B = gray ( $\eta$ ,  $\text{Co}_3\text{W}_3\text{C}$ ) phase; and Spot C = black (yttrium oxide) phase.

Figure 11 shows the microstructure of the consolidated WC-Co-TaC-NbC composites with 5 wt% Ni addition and different wt%  $\text{Y}_2\text{O}_3$ : 2.5 wt% (Figure 11a), 5 wt% (Figure 11b), 7.5 wt% (Figure 11c) and 10 wt% (Figure 11d). It can be observed that the microstructure consisted mainly of three phases, white (WC base), gray ( $\eta$ ,  $\text{Co}_3\text{W}_3\text{C}$ ) and black ( $\text{Y}_2\text{O}_3$ ). The  $\text{Y}_2\text{O}_3$  particles were homogeneously distributed across the WC matrix composite, and the area fraction increased as the wt%  $\text{Y}_2\text{O}_3$  increased. Figure 12 shows the area fraction of the three phases existing after the consolidation of the WC-based composite with 5 wt% Ni addition and at different percentages of added  $\text{Y}_2\text{O}_3$ . At 2.5 wt%  $\text{Y}_2\text{O}_3$ , the fractions of WC and  $\text{Co}_3\text{W}_3\text{C}$  were almost equal, at about 42% each. This ratio was changed with the increase of the  $\text{Y}_2\text{O}_3$  to 5, 7.5 and 10 wt%. It can be observed that the addition of the 5 wt% Ni enhanced the densification process, as noted by the higher relative density of the composites with the Ni addition relative to that free of Ni. This can be attributed to the low melting point of Ni (1453 °C), which improves the liquid phase sintering of the composites. as the liquid Ni + Co spread around the WC base composite and filled the empty spaces between the cold-compacted powder. Figure 13 shows the EDS analysis of the consolidated WC composites with 5 wt% Ni and 5 wt%  $\text{Y}_2\text{O}_3$ . The EDS analysis clearly

indicated the co-existence of 5 wt% Ni with Co to form the binding phase. It can be noted that the Ni existed in the gray phase.



**Figure 11.** SEM micrographs of the consolidated WC-Co-TaC-NbC samples with 5 wt% Ni and different wt%  $Y_2O_3$ : (a) 2.5 wt%  $Y_2O_3$ , (b) 5 wt%  $Y_2O_3$ , (c) 7.5 wt%  $Y_2O_3$ , (d) 10 wt%  $Y_2O_3$ .



**Figure 12.** Bar chart for the area fraction of the three phases: WC (white phase),  $Co_3W_3C$  (gray phase), and  $Y_2O_3$  (black phase), calculated using image analysis of the SEM micrographs shown in Figure 11.

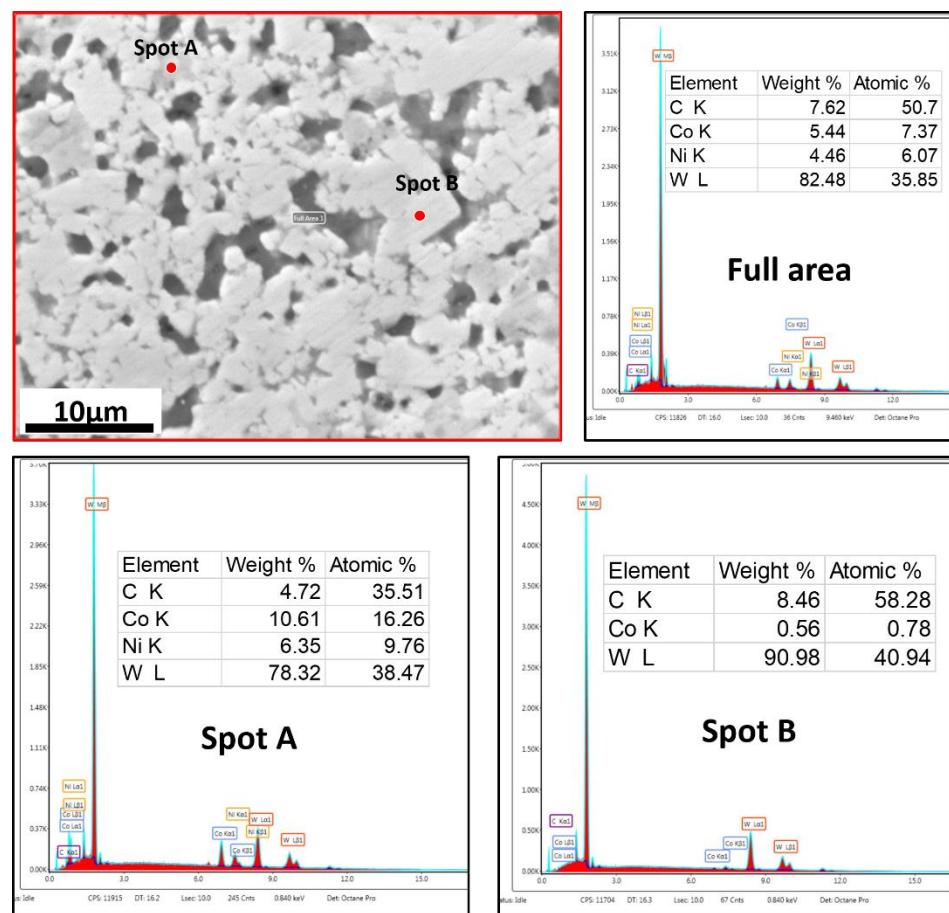
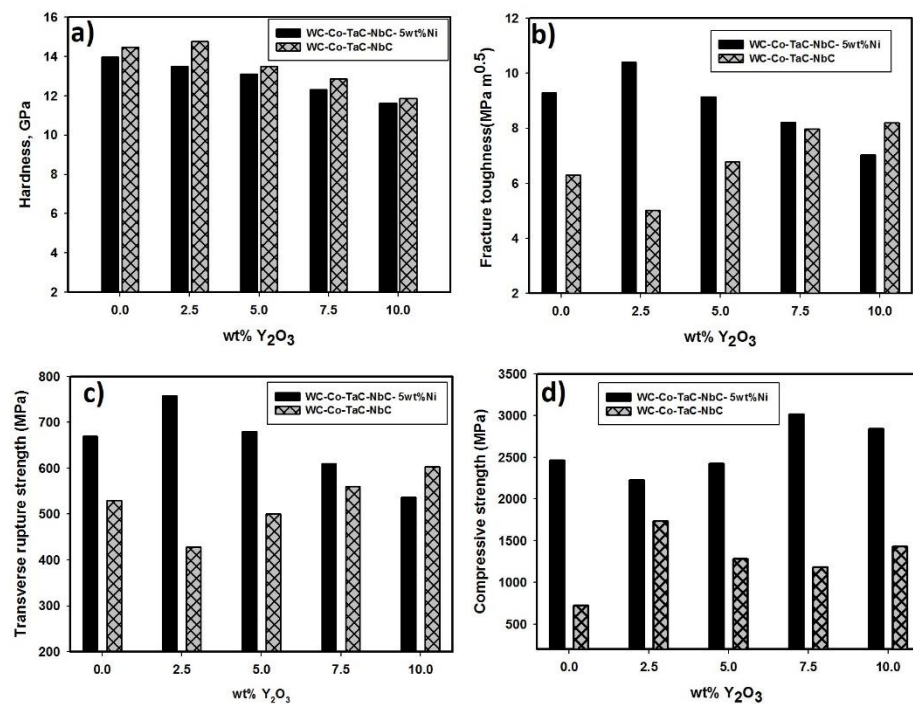


Figure 13. EDS analysis of the consolidated WC-Co-TaC-NbC-5 wt% Ni with 5 wt%  $Y_2O_3$ .

### 3.4. Mechanical Properties

Many applications of WC-based composites depend on the hardness and fracture toughness [27]. Fracture toughness strongly depends on the crack propagation resistance [38]. The conventional plain strain fracture toughness testing requires considerable effort; in particular, precracking of specimens has remained a serious obstacle [38]. Thus, an easy access to the fracture toughness is required for WC-based composite development and characterization. The industrially available cemented carbide alloy WC-6.5%Co possesses hardness of about 14 GPa and fracture toughness of  $11 \text{ MPa m}^{0.5}$  [37–40]. The currently developed WC-based composites have been characterized in terms of Vickers hardness, fracture toughness, TRS and compressive strength. Figure 14a–d shows the mechanical properties of the consolidated composites with and without 5 wt% Ni at the different  $Y_2O_3$  contents. From the Vickers hardness results, which were measured using a 30 Kg load (Figure 14a), it can be observed that the hardness exceeded the value of 14 GPa in some samples, especially those without the Ni addition. The addition of 5 wt% Ni resulted in the reduction of the hardness of the consolidated WC-based composites at all  $Y_2O_3$  contents. This can be attributed to the soft nature of Ni relative to the other constituents of the consolidated WC-based composites. As a result, this allowed the consolidated WC-based composites to afford a large amount of deformation upon hardness indentation. It can be noted also that increasing the content of  $Y_2O_3$  reduced the hardness values slightly, and this can be attributed to the increase of the apparent porosity, as well as the disconnection of the WC-based composite matrix by increasing  $Y_2O_3$  content, as can be observed in the microstructure (Figures 8 and 11).



**Figure 14.** Mechanical properties of the consolidated composites with and without 5 wt% Ni at different Y<sub>2</sub>O<sub>3</sub> contents. (a) Hardness, (b) fracture toughness, (c) transverse rupture strength, (d) compressive strength.

Fracture toughness was determined by applying the Vickers indentation on the polished surface of all the consolidated WC-based composites. Crack patterns developed from the indentation fracture at an applied load of 30 kg for the consolidated WC composites, both halfpenny and palmqvist cracks, as presented in Table 3. The samples without Ni addition showed half-penny cracks at the lower wt% Y<sub>2</sub>O<sub>3</sub> up to 5 wt% and then showed palmqvist crack up to 10 wt%. While the samples with 5 wt%Ni showed palmqvist cracks at all Y<sub>2</sub>O<sub>3</sub> contents. By applying the indentation fracture equations on both crack types for the different WC based composites the values of  $K_{IC}$  can be obtained [31].

**Table 3.** Fracture toughness and crack type developed for the sintered alloys.

Composite/ Y <sub>2</sub> O <sub>3</sub> .wt%	(WC-Co-TaC-NbC)	WC-Co-TaC-NbC-5wt%Ni
0	Halfpenny	Palmqvist
2.5	Halfpenny	Palmqvist
5	Halfpenny	Palmqvist
7.5	Palmqvist	Palmqvist
10	Palmqvist	Palmqvist

Figure 14b shows the calculated  $K_{IC}$  values plotted against the Y<sub>2</sub>O<sub>3</sub> content for the consolidated composites with and without 5 wt% Ni. It can be observed that the addition of 5 wt% Ni significantly improved the fracture toughness, especially with a lower content of Y<sub>2</sub>O<sub>3</sub>. The maximum value of fracture toughness (~11 MPa m<sup>0.5</sup>) was obtained in the sample that contained 5 wt% Ni and 2.5 wt% Y<sub>2</sub>O<sub>3</sub>. This can be attributed to the optimum densification of the matrix composite and the homogenous dispersion of the Y<sub>2</sub>O<sub>3</sub>. On the other hand, the minimum fracture toughness value was recorded for the 2.5 wt% Y<sub>2</sub>O<sub>3</sub> sample, which could be due to the formation of the brittle η-phase, as observed in the XRD results (Figure 6), which might result in a carbon-deficient environment and reduce the

volume fraction of the Co cementing phase, which would lower the fracture toughness value. This result is in good agreement with the result reported by Elkady [27]. The fracture toughness of the samples without the Ni addition increased with the increase of the  $Y_2O_3$  content, and this was a good match with the hardness results. It is known that there is an inverse relation between fracture toughness and hardness [31]. The decrease in the hardness was attributed to the increase of the apparent porosity with the increase of the  $Y_2O_3$  content. This porosity can play as crack arrester if the matrix is very well bonded and has a fine grain structure. Both factors can enhance the crack-propagation resistance and increase the fracture toughness. The fracture toughness values of the samples containing 5 wt% Ni decreased with increasing  $Y_2O_3$  content. This trend is in good agreement with the grain size of the WC and the mean-free path of the binder, where fracture toughness ( $K_{IC}$ ) of the cemented carbide is decreased as the binder phase volume fraction, carbide grain size and binder-phase mean-free path are decreased. The mean-free path, which is the average thickness of the binder between the WC grains, greatly depends on the binder content and the size of the WC grains. Increasing the  $Y_2O_3$  particles added at the expense of the base WC composite results in a decrease in the Co content, which decreases the thickness of the binder-free path, while increased carbide contiguity causes decreases in the fracture toughness.

The strength of the materials fabricated by the powder metallurgy (PM) technique usually is determined by the TRS through a bending test. This is one of the most traditional and common tests for measuring the strength of a brittle ceramic materials. It is a low-cost and versatile method to assess the strength and quality of a composite material [41]. The TRS is widely estimated in cemented carbides to evaluate their ability to bear an external load. Therefore, the TRS of cemented carbides sensitively depends on two major factors. The first is an extrinsic flaw where the fracture is initiated, and the second is an intrinsic resistance to propagate the crack. These defects have been shown to be voids, inclusions, abnormally large WC grains, segregated areas or lakes of the binder phase. The effect of these flaws on the TRS is dependent on the loading condition during the test. Generally, commercial WC-(3–15) wt% Co shows brittle fracture behavior [42]. Figure 14c presents the effect of  $Y_2O_3$  content on the TRS of the consolidated WC-based composites with and without 5 wt% Ni. It is clear that the maximum value of TRS was obtained from the sample that contained both 5 wt% Ni and 2.5 wt%  $Y_2O_3$ , while the sample with the same  $Y_2O_3$  content and without Ni showed the minimum TRS value. This result is in agreement with the fracture toughness results, which confirms the harmful effect of the  $\eta$ -phase  $Co_3W_3C$  on the fracture toughness and TRS as a brittle phase that can reduce the resistance for crack propagation. Recalling the XRD results (Figure 6), it can be observed that the peaks of the  $\eta$ -phase  $Co_3W_3C$  were pronounced in the composite of 2.5 wt%  $Y_2O_3$  without Ni, while the peaks are almost gone in that with the addition of 5 wt% Ni. On the other hand, increasing the  $Y_2O_3$  content with the existence of the 5 wt% Ni resulted in a reduction of the TRS, but it still was higher than those without Ni, especially up to 7.5 wt%  $Y_2O_3$ .

The behavior of the axial compressive strength as a function of the  $Y_2O_3$  content for the consolidated WC-based composites with and without 5 wt% Ni is shown in Figure 14d. It can be observed that the compressive strength of the composites containing 5 wt% Ni had a significantly higher compressive strength at all percentages of  $Y_2O_3$ . This can be attributed to the ductile behavior of Ni, which allows high resistance to compressive stress. The presence of Ni, in addition to Co, stabilized the relatively ductile fcc cobalt phase, retarding the cobalt transformation to the less ductile hcp phase. The compressive strength of the composite samples without the Ni addition increased by adding 2.5 wt%  $Y_2O_3$ , which could be due to the existence of the brittle  $\eta$ -phase  $Co_3W_3C$ , and then decreased again due to the high percentage of the apparent porosity. On the other hand, increasing the  $Y_2O_3$  content in the composites with 5 wt% Ni resulted in an increase of the compressive strength, which can be attributed to the increase in the ductile binder material and the increase in the porosity that might allow high compressibility in presence of the ductile phase.

It should be mentioned here that both the TRS and the fracture toughness of the WC-based composites were directly proportional to the  $Y_2O_3$  content, beginning at 2.5%. They increased with the increase in the  $Y_2O_3$  content, with the maximum value achieved at the 10 wt%  $Y_2O_3$  in both cases. The  $Y_2O_3$  particles were of a very fine particle size (2–3  $\mu\text{m}$ ) relative to the matrix phase, which was expected to be refined more by the mechanical milling process. Thus, the increase in this phase fraction increased the fine particle size phase fraction in the whole composite, and this enhanced both properties due to the grain size reduction. Although the addition of 5 wt% Ni reversed the behavior, as the maximum values were obtained at 2.5 wt%  $Y_2O_3$  and then both properties decreased, the values were still higher than that without the Ni addition for 5 and 7.5 wt%  $Y_2O_3$ . This reduction can be understood with respect to the ductile state of Ni. The other two mechanical properties (hardness and compressive strength) both were significantly affected by the porosity percentage, which explains why they were decreased by the increase in the wt%  $Y_2O_3$  content, and the addition of 5 wt% Ni enhanced the properties due to the increase in the densification.

#### 4. FSW Tool for High-Softening-Temperature Materials

Friction stir welding (FSW) is a solid-state welding process [43–46] that has been used at the laboratory scale for welding both low-softening-temperature materials (Al, Cu, Mg) [45–48] and high-softening-temperature materials (Ti, Ni, steel alloys) [49–51]. However, in terms of industrial applications, only low-softening-temperature materials find their way into a large number of applications, such as shipbuilding, railway, aerospace and automotive [44]. The welding mechanism in the FSW process is based on the heat generated due to the severe friction between the FSW tool and the workpiece. This heat softens the workpiece material around the tool, which allows the tool to travel along the joint line and generate the joint in a solid state. The FSW is considered a thermomechanical process in which the required heat for the high-temperature deformation is generated by friction between the FSW tool and the surrounding material. The material used to manufacture the FSW tools has to be of high strength at high temperatures, and possess high wear resistance to afford the severe conditions experienced during the FSW process [52]. A material used for FSW of low-softening-temperature materials is hot work tool steel [52,53]. This type of tool steel is characterized by easy availability and machinability, thermal fatigue resistance and wear resistance, and can be used for FSW of aluminum alloys at low cost and for hundreds of meters without significant deterioration [52,54]. On the other hand, during FSW of high-softening-temperature materials, the tool life is strongly affected by the peak temperature and the applied stresses [55]. The mainly available tool materials are PCBN [56], W-Re [49] and WC-based [50,57]. Both PCBN and W-Re are very expensive and require high-stiffness FSW machines for the minimum runout required to avoid tool fracture [52]. Commercially available WC-based materials suffer from a high wear rate and low fracture toughness [55]. In this context, Tiwar et al. [55] investigated the performance of two WC-Co tools (WC-6 wt% Co and WC-10 wt% Co) in FSW of DH36 steel butt joints. They reported that the tool made of WC-6 wt% was degraded after one weld of 250 mm due to intergranular failure caused by the separation of the tungsten carbide grains, which promoted further cracks inside the tool. The tool made of WC-10 wt% was degraded after 5 welds of 250 mm each due to progressive wear, and was strongly affected by the process temperatures. Thus, it is highly necessary to develop low-cost and durable tools to widen the industrial applications of the process for welding of high-softening-temperature materials such Ni-based alloys, steel alloys and titanium alloys.

Based on the current investigation and the results obtained, the WC-based composite with the addition of 5 wt% Ni had superior mechanical properties to that without Ni, especially the fracture toughness, TRS and compressive strength. The high fracture toughness and TRS are required for the FSW tool materials of high-softening-temperature materials. Accordingly, the WC composite with 2.5 wt%  $Y_2O_3$  and 5 wt% Ni was selected to manufacture the FSW tools in the current study. Figure 15 presents SEM micrographs of this composite at different magnifications that clearly show the full densification and

the homogeneous distribution of the added  $Y_2O_3$  particles. In addition, it can be observed that the grain size of the WC matrix phase is fine, and the matrix is very well bonded and connected. To manufacture the FSW tools, two cylindrical parts 23 mm in diameter and 30 to 40 mm in length (Figure 16a) were manufactured using the same consolidation procedures carried out in this work. The parts were then grinded to the required geometry for FSW tools and inserted into heat-treated tool steel holders to be fixed in the FSW machine (Figure 16a). The FSW tools were used in the welding of Ni base alloy and steel alloys several times. More than 300 cm of butt joints in the Ni base alloy were produced with more than 16 plunges, and 200 cm of butt joints in carbon steel and about 10 plunges with the same tool. Figure 16b shows the FSW tool during the welding process and the high temperatures it experienced during the process. Figure 17 show some top-view images of the welded Ni base alloy (Figure 17a) and carbon steel (Figure 17b). The FSW tool after a number of welding joints is pictured in Figure 17c. It can be observed that no wear or deterioration can be seen in the WC tool after several FSW experiments conducted on both Ni base and steel alloys. This implies that the currently developed WC-based composites are of high potential for the commercial FSW of high-softening-temperature materials with a low cost and long life. These WC-based composites can be applied at low cost in the FSW of high-softening-temperature material such as steel alloys and nickel-based alloys. In addition, they can be applied in other friction-based applications [58,59].

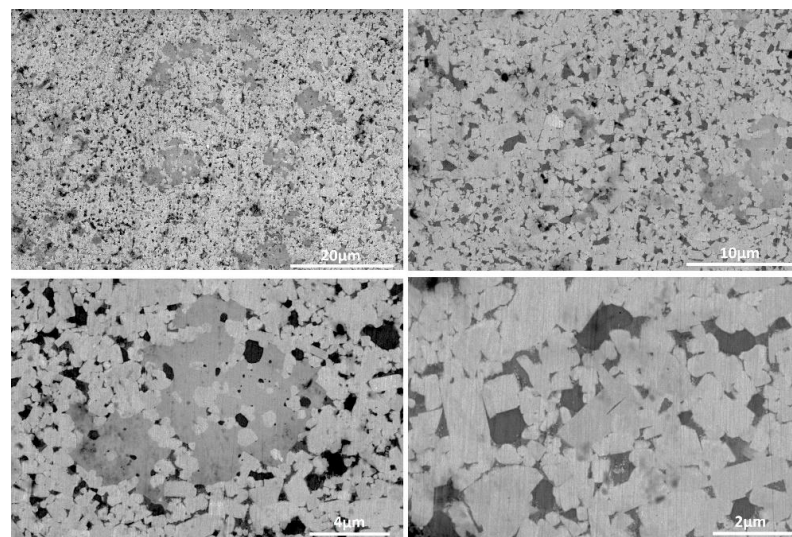


**Figure 15.** SEM micrographs of the consolidated WC-Co-TaC-NbC with 5 wt% Ni and 2.5 wt%  $Y_2O_3$  at different magnifications.



**Figure 16.** The manufactured cylindrical parts from the WC-based composites with 5 wt% Ni and 2.5 wt%  $Y_2O_3$  for the FSW tool applications. (a) Images of the parts after consolidation, grinding for the required geometries and insertion in the tool steel holder. (b) The FSW tool during the welding of the Ni base alloy.

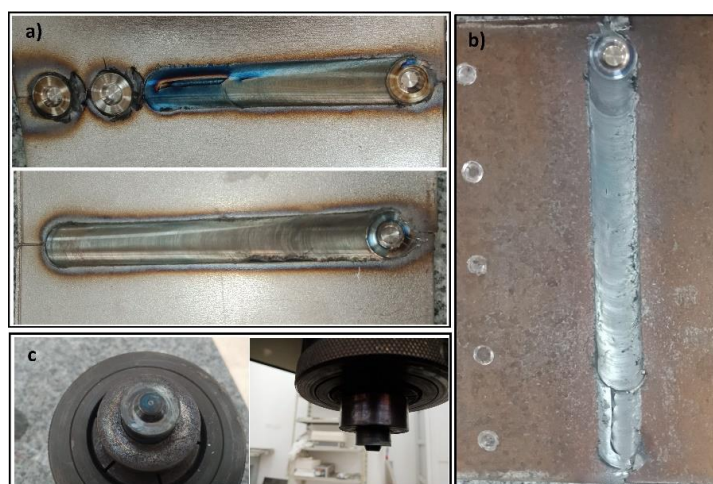


**Figure 17.** Top views of the welded materials using the produced WC-based composite tool material (WC-Co-TaC-NbC with 2.5 wt%  $Y_2O_3$  and 5 wt% Ni). (a) Ni base alloy, (b) carbon steel, (c) the FSW tool after several FSW experiments.

## 5. Conclusions

Two series of WC-Co-TaC-NbC and WC-Co-TaC-NbC-5 wt% Ni composites with different additions of  $Y_2O_3$  from 0–10 wt% were produced and characterized. Based on the obtained results, the following conclusions can be outlined:

1. The consolidation process applied to the WC-based composites resulted in a relative density of up to 97%, which was enhanced by the 5 wt% Ni addition.
2. Upon the sintering process, the  $Co_3W_3C$   $\eta$ -phase was formed, and its formation was slightly reduced by the addition of 5 wt% Ni and 2.5 wt%  $Y_2O_3$ .
3. The microstructure of the consolidated composites consisted of a very well-connected WC matrix, with homogenous dispersion of the  $Y_2O_3$  particles at the lower  $Y_2O_3$  content (up to 5 wt%) which retarded the grain growth during sintering.
4. The addition of 5 wt% Ni significantly enhanced the fracture toughness (max. of  $10.4 \text{ MPa} \sqrt{m}$ ), the transverse rupture strength (max. of 758 Mpa) and the compressive strength (max. of 3013 MPa). On the other hand, only the hardness was slightly reduced for all  $Y_2O_3$  contents; for example, at 0 wt%  $Y_2O_3$ , the hardness was reduced from 1425 MPa to 1398 MPa.
5. The WC-Co-TaC-NbC with 2.5 wt%  $Y_2O_3$  and 5 wt% Ni was selected to manufacture friction stir welding tools, which were successfully used for the FSW of Ni base alloy and carbon steel, with more than 25 plunges and more than 500 cm of butt joints. This can be a cost-effective tool material for the FSW of high-softening-temperature materials such as steel and nickel-based alloys.

**Author Contributions:** Conceptualization, M.M.Z.A. and O.A.E.; data curation, O.A.E.; formal analysis, W.S.B.; funding acquisition, N.A.A.; investigation, W.S.B., A.Y.A.M. and O.A.E.; methodology, M.M.Z.A., W.S.B. and A.Y.A.M.; resources, A.Y.A.M. and N.A.A.; supervision, M.M.Z.A. and O.A.E.; validation, A.Y.A.M.; writing-original draft, M.M.Z.A., O.A.E. and W.S.B.; writing-review and editing, M.M.Z.A. All authors have read and agreed to the published version of the manuscript.

**Funding:** This research received no external funding.

**Institutional Review Board Statement:** Not applicable.

**Informed Consent Statement:** Not applicable.

**Data Availability Statement:** The data presented in this study are available on request from the corresponding author. The data are not publicly available due to the extremely large size.

**Conflicts of Interest:** The authors declare no conflict of interest.

## References

1. Ma, J.; Zhu, S.; Ouyang, C. Two-Step Hot-Pressing Sintering of Nanocomposite WC-MgO Compacts. *J. Eur. Ceram. Soc.* **2011**, *31*, 1927–1935. [[CrossRef](#)]
2. Mukhopadhyay, A.; Chakravarty, D.; Basu, B. Spark Plasma-Sintered WC-ZrO<sub>2</sub>-Co Nanocomposites with High Fracture Toughness and Strength. *J. Am. Ceram. Soc.* **2010**, *93*, 1754–1763. [[CrossRef](#)]
3. Kim, H.C.; Shon, I.J.; Yoon, J.K.; Doh, J.M. Consolidation of Ultra Fine WC and WC-Co Hard Materials by Pulsed Current Activated Sintering and Its Mechanical Properties. *Int. J. Refract. Met. Hard Mater.* **2007**, *25*, 46–52. [[CrossRef](#)]
4. Sivaprahasam, D.; Chandrasekar, S.B.; Sundaresan, R. Microstructure and Mechanical Properties of Nanocrystalline WC-12Co Consolidated by Spark Plasma Sintering. *Int. J. Refract. Met. Hard Mater.* **2007**, *25*, 144–152. [[CrossRef](#)]
5. Kim, C.S.; Massa, T.R.; Rohrer, G.S. Modeling the Relationship between Microstructural Features and the Strength of WC-Co Composites. *Int. J. Refract. Met. Hard Mater.* **2006**, *24*, 89–100. [[CrossRef](#)]
6. Schreiber, J. *Springer Series in Materials Science 11*; Springer Nature Switzerland AG: Cham, Switzerland, 2010; Volume 190, ISBN 9783319005232.
7. Xiao, D.H.; He, Y.H.; Song, M.; Lin, N.; Zhang, R.F. Y<sub>2</sub>O<sub>3</sub>- and NbC-Doped Ultrafine WC-10Co Alloys by Low Pressure Sintering. *Int. J. Refract. Met. Hard Mater.* **2010**, *28*, 407–411. [[CrossRef](#)]
8. Agrawal, D.; Cheng, J.; Seegopaul, P.; Gao, L. Grain Growth Control in Microwave Sintering of Ultrafine WC-Co Composite Powder Compacts. *Powder Metall.* **2000**, *43*, 15–16.
9. Azcona, I.; Ordóñez, A.; Sánchez, J.M.; Castro, F. Hot Isostatic Pressing of Ultrafine Tungsten Carbide-Cobalt Hardmetals. *J. Mater. Sci.* **2002**, *37*, 4189–4195. [[CrossRef](#)]
10. Chen, J.; Liu, W.; Deng, X.; Wu, S. Tool Life and Wear Mechanism of WC-5TiC-0.5VC-8Co Cemented Carbides Inserts When Machining HT250 Gray Cast Iron. *Ceram. Int.* **2016**, *42*, 10037–10044. [[CrossRef](#)]
11. Seleman, M.M.E.; Ahmed, M.M.Z.; Ataya, S.; Mohamed, M.; El-Sayed, S.; Mohamed, M.Z.; Ahmed, S.A. Microstructure and Mechanical Properties of Hot Extruded 6016 Aluminum Alloy/Graphite Composites. *J. Mater. Sci. Technol.* **2018**, *34*, 1580–1591. [[CrossRef](#)]
12. Duman, D.; Gökçe, H.; Çimenoglu, H. Synthesis, Microstructure, and Mechanical Properties of WC-TiC-Co Ceramic Composites. *J. Eur. Ceram. Soc.* **2012**, *32*, 1427–1433. [[CrossRef](#)]
13. Fang, Z.Z.; Wang, X.; Ryu, T.; Hwang, K.S.; Sohn, H.Y. Synthesis, Sintering, and Mechanical Properties of Nanocrystalline Cemented Tungsten Carbide—A Review. *Int. J. Refract. Met. Hard Mater.* **2009**, *27*, 288–299. [[CrossRef](#)]
14. Yu, H.; Li, W.N.; Jiang, X.Q.; Jiao, P.H. Effect of VC, TaC and NbC Additions on Microstructure and Properties of Ultrafine WC-10%Co Cemented Carbides. *Appl. Mech. Mater.* **2013**, *320*, 281–286. [[CrossRef](#)]
15. Xiao, D.H.; He, Y.H.; Luo, W.H.; Song, M. Effect of VC and NbC Additions on Microstructure and Properties of Ultrafine WC-10Co Cemented Carbides. *Trans. Nonferrous Met. Soc. China (Engl. Ed.)* **2009**, *19*, 1520–1525. [[CrossRef](#)]
16. Liu, S.; Huang, Z.L.; Liu, G.; Yang, G. Bin Preparing Nano-Crystalline Rare Earth Doped WC/Co Powder by High Energy Ball Milling. *Int. J. Refract. Met. Hard Mater.* **2006**, *24*, 461–464. [[CrossRef](#)]
17. Lin, N.; Jiang, Y.; Zhang, D.F.; Wu, C.H.; He, Y.H.; Xiao, D.H. Effect of Cu, Ni on the Property and Microstructure of Ultrafine WC-10Co Alloys by Sinter-Hipping. *Int. J. Refract. Met. Hard Mater.* **2011**, *29*, 509–515. [[CrossRef](#)]
18. Yajiang, L.; Zengda, Z.; Xiao, H.; Tao, F.; Xinghong, W. A Study on Microstructure in the Brazing Interface of WC-TiC-Co Hard Alloys. *Int. J. Refract. Met. Hard Mater.* **2002**, *20*, 169–173. [[CrossRef](#)]
19. Huang, S.G.; Liu, R.L.; Li, L.; Van der Biest, O.; Vleugels, J. NbC as Grain Growth Inhibitor and Carbide in WC-Co Hardmetals. *Int. J. Refract. Met. Hard Mater.* **2008**, *26*, 389–395. [[CrossRef](#)]
20. Zhou, W.; Xiong, J.; Wan, W.; Guo, Z.; Lin, Z.; Huang, S.; Tang, L.; Zhong, H. The Effect of NbC on Mechanical Properties and Fracture Behavior of WC-10Co Cemented Carbides. *Int. J. Refract. Met. Hard Mater.* **2015**, *50*, 72–78. [[CrossRef](#)]
21. Venkateswaran, T.; Sarkar, D.; Basu, B. Tribological Properties of WC-ZrO<sub>2</sub> Nanocomposites. *J. Am. Ceram. Soc.* **2005**, *88*, 691–697. [[CrossRef](#)]
22. Su, W.; Sun, Y.; Liu, J.; Feng, J.; Ruan, J. Effects of Ni on the Microstructures and Properties of WC-6Co Cemented Carbides Fabricated by WC-6(Co, Ni) Composite Powders. *Ceram. Int.* **2015**, *41*, 3169–3177. [[CrossRef](#)]
23. Tarragó, J.M.; Roa, J.J.; Valle, V.; Marshall, J.M.; Llanes, L. Fracture and Fatigue Behavior of WC-Co and WC-CoNi Cemented Carbides. *Int. J. Refract. Met. Hard Mater.* **2015**, *49*, 184–191. [[CrossRef](#)]
24. Shi, K.H.; Zhou, K.C.; Li, Z.Y.; Zhang, D.; Zan, X.Q. Microstructure and Formation Process of Ni-Pool Defect in WC-8Ni Cemented Carbides. *Trans. Nonferrous Met. Soc. China* **2015**, *25*, 873–878. [[CrossRef](#)]
25. Sha, L. Study on Rare-Earth Doped Cemented Carbides in China. *Int. J. Refract. Met. Hard Mater.* **2009**, *27*, 528–534. [[CrossRef](#)]
26. Pan, Q. Effects of Rare Earth Oxides on the Properties of WC-Co Cemented Carbide. *Rare Met. Mater. Eng.* **1993**, *41*, 22–35.
27. El-kady, O.A.M. Effect of Nano-Yttria Addition on the Properties of WC/Co Composites. *Mater. Des.* **2013**, *52*, 481–486. [[CrossRef](#)]
28. Qin, Y.; Peng, Y.; Tian, Y.; Luo, L.; Ma, Y.; Zan, X. Effect of Y<sub>2</sub>O<sub>3</sub> on Microstructure and Mechanical Properties of WC-Co-Cemented Carbides Prepared via Solid-Liquid Doping Method and Spark Plasma Sintering. *Mater. Today Commun.* **2020**, *24*, 101096. [[CrossRef](#)]
29. Yang, Y.; Luo, L.; Zan, X.; Zhu, X.; Zhu, L.; Wu, Y. International Journal of Refractory Metals Synthesis of Y<sub>2</sub>O<sub>3</sub>-Doped WC-Co Powders by Wet Chemical Method and Its Effect on the Properties of WC-Co Cemented Carbide Alloy. *Int. J. Refract. Metals Hard Mater.* **2020**, *92*, 105324. [[CrossRef](#)]

30. Li, J.; Cheng, J.; Wei, B.; Chen, P. Preparation and Performance of Ultra Fine Grained WC-10Co Alloys With. *Ceram. Int.* **2019**, *45*, 3969–3976. [[CrossRef](#)]
31. Shetty, D.K.; Wright, I.G.; Mincer, P.N.; Clauer, A.H. Indentation fracture of WC-Co Cermets. *J. Mater. Sci.* **1985**, *20*, 1873–1882. [[CrossRef](#)]
32. Ewais, E.M.M.; Besisa, D.H.A.; Zaki, Z.I.; Kandil, A.E.H.T. Tailoring of Functionally Graded Zirconia-Mullite/Alumina Ceramics. *J. Eur. Ceram. Soc.* **2012**, *32*, 1561–1573. [[CrossRef](#)]
33. El-Eskandarany, M.S. *Mechanical Alloying Energy Storage, Protective Coatings, and Medical Applications*, 3rd ed.; William Andrew: Norwich, NY, USA, 2020; ISBN 9780128181805.
34. El-eskandarany, M.S.; Mahday, A.A.; Ahmed, H.A.; Amer, A.H. Synthesis and Characterizations of Ball-Milled Nanocrystalline WC and Nanocomposite WC-Co Powders and Subsequent Consolidations. *J. Alloys Compd.* **2000**, *312*, 315–325. [[CrossRef](#)]
35. Riedel, R.; Chen, I.W. *Ceramics Science and Technology*; Wiley: Hoboken, NJ, USA, 2008; ISBN 9783527313204.
36. Fang, Z.Z.; Eso, O.O. Liquid Phase Sintering of Functionally Graded WC-Co Composites. *Scr. Mater.* **2005**, *52*, 785–791. [[CrossRef](#)]
37. Silva, A.G.P.; Schubert, W.D.; Lux, B. The Role of the Binder Phase in the WC-Co Sintering. *Mater. Res.* **2001**, *4*, 59–62.
38. Anderson, T.L. *Fracture Mechanics Fundamentals and Applications*, 3rd ed.; Taylor & Francis Group: Abingdon, UK, 2005; ISBN 9781420058215.
39. Bouaouadja, N.; Hamidouche, M.; Osmani, H.; Fantozzi, G. Fracture Toughness of WC-Co Cemented Carbides at Room Temperature. *J. Mater. Sci. Lett.* **1994**, *13*, 17–19. [[CrossRef](#)]
40. Spiegler, R.; Schmauder, S.; Sigl, L.S. Fracture Toughness Evaluation of WC-Co Alloys by Indentation Testing. *J. Hard Mater.* **1990**, 1147–1158.
41. Quinn, G.D.; Morrell, R. Design Data for Engineering Ceramics: A Review of the Flexure Test. *J. Am. Ceram. Soc.* **1991**. [[CrossRef](#)]
42. Hewitt, S.A. Consolidation of WC-Co Nanocomposites Synthesised By Mechanical Alloying. Ph.D. Thesis, University of Wolverhampton, Wolverhampton, UK, 2009.
43. Mishra, R.S.; Ma, Z.Y. Friction Stir Welding and Processing. *Mater. Sci. Eng. R* **2005**, *50*, 1–78. [[CrossRef](#)]
44. Threadgill, P.L.; Leonard, A.J.; Shercliff, H.R.; Withers, P.J. Friction Stir Welding of Aluminium Alloys. *Int. Mater. Rev.* **2009**, *54*, 49–93. [[CrossRef](#)]
45. Ahmed, M.M.Z.; Wynne, B.P.; El-Sayed Seleman, M.M.; Rainforth, W.M. A comparison of crystallographic texture and grain structure development in aluminum generated by friction stir welding and high strain torsion. *Mater. Des.* **2016**, *103*, 259–267. [[CrossRef](#)]
46. Ahmed, M.M.Z.; Seleman, M.M.E.; Zidan, Z.A.; Ramadan, R.M.; Ataya, S.; Alsaleh, N.A. Microstructure and Mechanical Properties of Dissimilar Friction Stir Welded AA2024-T4/AA7075-T6 T-Butt Joints. *Metals* **2021**, *11*, 128. [[CrossRef](#)]
47. Ahmed, M.M.Z.; Ataya, S.; Seleman, M.M.E.; Allam, T. Grain Structure, Crystallographic Texture, and Hardening Behavior of Dissimilar Friction Stir Welded AA5083-O And AA5754-H14. *Metals* **2021**, *11*, 181. [[CrossRef](#)]
48. Ahmed, M.M.Z.; Ataya, S.; Seleman, M.M.E.; Mahdy, A.M.A.; Alsaleh, N.A.; Ahmed, E. Heat Input and Mechanical Properties Investigation of Friction Stir Welded AA5083/AA5754 and AA5083/AA. *Metals* **2021**, *11*, 68. [[CrossRef](#)]
49. Ahmed, M.M.Z.; Wynne, B.P.; Martin, J.P. Effect of Friction Stir Welding Speed on Mechanical Properties and Microstructure of Nickel Based Super Alloy Inconel 718. *Sci. Technol. Weld. Join.* **2013**, *18*, 680–687. [[CrossRef](#)]
50. Ahmed, M.M.Z.; Seleman, M.M.E.S.; Shazly, M.; Attallah, M.M.; Ahmed, E. Microstructural Development and Mechanical Properties of Friction Stir Welded Ferritic Stainless Steel AISI. *J. Mater. Eng. Perform.* **2019**, *28*, 6391–6406. [[CrossRef](#)]
51. Refat, M.; Elashery, A.; Toschi, S.; Ahmed, M.M.Z.; Morri, A.; El-Mahallawi, I.; Ceschini, L. Microstructure, Hardness and Impact Toughness of Heat-Treated Nanodispersed Surface and Friction Stir-Processed Aluminum Alloy AA. *J. Mater. Eng. Perform.* **2016**, *25*, 5087–5101. [[CrossRef](#)]
52. Meilinger, A.; Torok, I. The Importance of Friction Stir Welding Tool. *Prod. Process. Syst.* **2013**, *6*, 25–34.
53. Ahmed, M.M.Z.; Ataya, S.; El-Sayed Seleman, M.M.; Ammar, H.R.; Ahmed, E. Friction Stir Welding of Similar and Dissimilar AA7075 and AA5083. *J. Mater. Process. Technol.* **2017**, *242*, 77–91. [[CrossRef](#)]
54. Ahmed, M.M.Z.; Wynne, B.P.; Rainforth, W.M.; Addison, A.; Martin, J.P.; Threadgill, P.L. Effect of Tool Geometry and Heat Input on the Hardness, Grain Structure, and Crystallographic Texture of Thick-Section Friction Stir-Welded Aluminium. *Metall. Mater. Trans. A Phys. Metall. Mater. Sci.* **2019**, *50*, 271–284. [[CrossRef](#)]
55. Tiwari, A. Tool Performance Evaluation of Friction Stir Welded Shipbuilding Grade DH36 Steel Butt Joints. *Int. J. Adv. Manuf. Technol.* **2019**, *103*, 1989–2005. [[CrossRef](#)]
56. Kangazian, J.; Shamanian, M. Microstructure and Mechanical Characterization of Incoloy 825 Ni-Based Alloy Welded to 2507 Super Duplex Stainless Steel through Dissimilar Friction Stir Welding. *Trans. Nonferrous Met. Soc. China* **2019**, *29*, 1677–1688. [[CrossRef](#)]
57. Ahmed, M.M.Z.; Ahmed, E.; Hamada, A.S.; Khodir, S.A.; El-Sayed Seleman, M.M.; Wynne, B.P. Microstructure and Mechanical Properties Evolution of Friction Stir Spot Welded High-Mn Twinning-Induced Plasticity Steel. *Mater. Des.* **2016**, *91*. [[CrossRef](#)]
58. Haneklaus, N.; Cionea, C.; Reuven, R.; Frazer, D.; Hosemann, P.; Peterson, P.F. Hybrid Friction Diffusion Bonding of 316L Stainless Steel Tube-to-Tube Sheet Joints for Coil-Wound Heat Exchangers. *J. Mech. Sci. Technol.* **2016**, *30*, 4925–4930. [[CrossRef](#)]
59. Zayed, E.M.; El-Tayeb, N.S.M.; Ahmed, M.M.Z.; Rashad, R.M. Development and Characterization of AA5083 Reinforced with SiC and Al<sub>2</sub>O<sub>3</sub> Particles by Friction Stir Processing. In *Engineering Design Applications*; Springer: Cham, Switzerland, 2019; Volume 92.